A Neuro-Fuzzy Approach for Medical Image Fusion

Sudeb Das* and Malay Kumar Kundu, *Senior Member, IEEE*

***Abstract*—This paper addresses a novel approach to the multimodal medical image fusion (MIF) problem, employing multiscale geometric analysis of the nonsubsampled contourlet transform and fuzzy-adaptive reduced pulse-coupled neural network (RPCNN). The linking strengths of the RPCNNs' neurons are adaptively set by modeling them as the fuzzy membership values, representing their significance in the corresponding source image. Use of the RPCNN with a less complex structure and having less number of parameters leads to computational efficiency—an important requirement of point-of-care health care technologies. The proposed scheme is free from the common shortcomings of the state-of-the-art MIF techniques: contrast reduction, loss of image fine details, and unwanted image degradations, etc. Subjective and objective evaluations show better performance of this new approach compared to the existing techniques.**

***Index Terms*—Artificial neural network, fuzzy logic, image analysis, image fusion (IF), medical imaging (MI).**

I. Introduction

NOWADAYS, we have various modalities of medical images. Different modalities of medical images reflect different information of human organs and tissues, and have their respective applications. A single modality of a medical image cannot provide comprehensive and accurate information. Therefore, it is necessary to correlate one modality of the medical image to another to obtain the relevant information. Moreover, the manual process of integrating several modalities of medical images is rigorous, time consuming, costly, subject to human error, and requires years of experience. Therefore, automatically combining multimodal medical images through image fusion (IF) has become the focus of imaging research and processing [1], [2].

In recent years, many IF and medical image fusion (MIF) techniques have been proposed by various researchers. It has been found that the pixel-level spatial domain methods usually lead to contrast reduction. Approaches based on intensity-hue-saturation, principal component analysis, and the Brovey transform offer better results, but suffer from spectral degradation. Pyramidal IF schemes fail to introduce any spatial orientation selectivity in the decomposition process, and hence often cause blocking effects [3], [4]. Most of the aforementioned schemes are modality specific with their own limitations [5]. The problem with the widely used wavelet transform (WT) is that it can preserve the spectral information efficiently but cannot express the spatial characteristics well [6]–[8]. As a result, WT-based fusion schemes fail to preserve the salient features of the source images efficiently and introduce artifacts and inconsistencies in the fused results [9]. Recently, to overcome these problems, many improved IF/MIF methods based on multiscale geometric analysis (MGA) tools (like curvelet, contourlet, and ripplet, etc.) have been proposed [9], [10]. However, measuring the importance/contribution of individual source image in the fused image, and finding an effective way of combining them is still an open problem.

In 1990, Eckhorn *et al.* introduced the linking field network model for the systems exhibiting the synchronous pulse bursts [11]. Modifications and variants of the linking field model for image processing applications became known as the pulse-coupled neural networks (PCNNs) [12]–[14]. The PCNN simulates the processing mechanism of cat's visual cortex and is characterized by global coupling and the pulse synchronization of neurons. The PCNN and its modified versions have been used in the IF/MIF domains by various researchers [3], [5], [15], [16]. Even though, PCNN-based IF/MIF methods outperform other conventional schemes, these approaches also suffer from several shortcomings: contrast reduction, loss of image fine details, and unwanted degradations, etc. Moreover, the PCNN has several parameters with complex structures, and optimal estimation of these parameters is a major limitation to automatization and generalization of PCNN. In most of the PCNN-based IF/MIF techniques, these parameters are kept the same and set as a constant. But, according to the human visual system (HVS), the responses to a region with the notable features are stronger than a region with nonnotable features. Thus, the parameters of PCNN's neurons should be related to the importance (significance) of the features of either the corresponding pixel (in a spatial domain) or the coefficient (in a transform domain) of the image [17]–[19]. But the problem remains: how to measure the importance (significance) of the pixel (coefficient) in the corresponding image. Therefore, we not only need a way to adaptively and automatically set the values of the parameters of the PCNN, but also to make the fusion scheme free from the common problems faced by the existing techniques [20]. This paper explores the use of fuzzy logic for building a simultaneous fusion and enhancement technique based on the HVS model to address the aforementioned problems. In this regard, the main contributions of this paper are as follows: 1) A novel MIF scheme employing nonsubsampled contourlet transform (NSCT) and reduced PCNN (RPCNN) with adaptive linking strengths based on the corresponding image's local features. 2) Following the subjectivity of HVS, fuzzy logic is used to enable

Manuscript received January 22, 2013; revised June 25, 2013; September 5, 2013; accepted September 12, 2013. Date of publication September 18, 2013; date of current version November 18, 2013. This work was supported by Machine Intelligence Unit, Indian Statistical Institute, Kolkata-108, India, (Internal Academic Project). *Asterisk indicates corresponding author.*

*S. Das is with the Machine Intelligence Unit, Indian Statistical Institute, 203 B.T. Road, Kolkata-108, India (e-mail: to.sudeb@gmail.com).

M. K. Kundu is with the Machine Intelligence Unit, Indian Statistical Institute, 203 B.T. Road, Kolkata-108, India (e-mail: malay@isical.ac.in).

Color versions of one or more of the figures in this paper are available online at http://ieeexplore.ieee.org.

the proposed scheme to produce high-quality fused images with higher contrast, more clarity, and more useful subtle detail information. 3) Without involving any prior training and trials, the less complex RPCNN having less number of parameters leads to computational efficiency, which is suitable for the real time image processing applications (like point-of-care health care technologies). Both subjective and objective performance evaluations were carried out and verified. Performance comparisons with state-of-the-art schemes show that the proposed method performs better.

The remainder of this paper is organized as follows. NSCT is described in Section II. In Section III, the RPCNN model is briefly reviewed. Section IV presents the proposed MIF scheme. Experimental results and comparisons are given in Section V, and we draw conclusion in Section VI.

II. Nonsubsampled Contourlet Transform

NSCT is a fully shift-invariant, multiscale, and multidirection expansion with fast implementability [21]. NSCT achieves the shift-invariance property [not present in contourlet transform (CNT)] by using the nonsubsampled pyramid filter bank (NSP) and the nonsubsampled directional filter bank (NSDFB).

A. Nonsubsampled Pyramid Filter Bank

NSP ensures the multiscale property of NSCT, and has no down-sampling or up-sampling, and hence is shift-invariant. It is constructed by the iterated two channel nonsubsampled filter bank (NSFB), and one low-frequency and one high-frequency image is produced at each NSP decomposition level. The subsequent NSP decomposition stages are carried out to decompose the low-frequency component available iteratively to capture the singularities in the image. As a result, NSP results in $k+1$ subimages (having the same size as that of the source image), which consist of one low-frequency image and k high-frequency images, where k denotes the number of decomposition levels.

B. Nonsubsampled Directional Filter Bank

The NSDFB is constructed by eliminating the downsamplers and upsamplers of the DFB [21]. This results in a tree composed of two-channel NSFBs. The NSDFB allows direction decomposition with l stages in high-frequency images from NSP at each scale, and produces 2^l directional subimages with the same size as the source image. Thus, NSDFB enables NSCT with the multidirection property and provides more precise directional detail information. The outputs of the first and second level filters are combined to get the directional frequency decompositions. The synthesis filter bank is obtained similarly. All the filter banks in the NSDFB-tree structure are obtained from a single NSFB with fan filters. To obtain multidirectional decomposition, the NSDFBs are iterated, and to get the next level decomposition, all the filters are upsampled by a quincunx matrix given by $\mathrm{QM} = [1 \quad 1; 1 \quad -1]$.

NSCT is obtained by combining the NSP and the NSDFB as described by Fig. 1. For further information on NSCT, see [21].

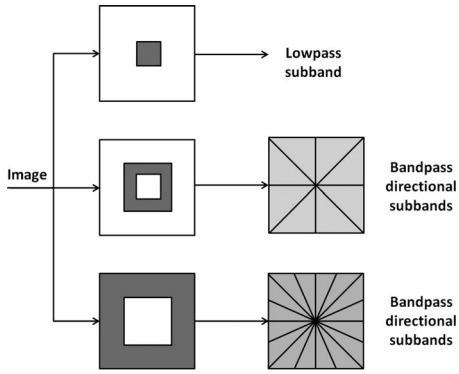

Fig. 1. NSFB structure that implements the NSCT.

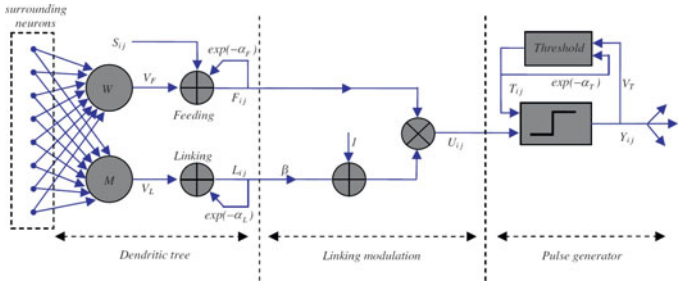

Fig. 2. Structure of PCNN.

In the proposed method, the decomposition parameter of NSCT is set at levels $= [1, 2, 2]$ and we use "*pyrexc*" and "*vk*" as the pyramid filter and orientation filter, respectively. With this decomposition configuration, the number of subband images obtained is 11. Each obtained subband is of the same size as the source medical image. This helps in finding the relationship between the different subbands, which is good for designing the fusion rule and helpful for avoiding the pseudo-Gibbs phenomenon. Moreover, NSCT has better frequency selectivity and regularity than the other MGA tools and is capable of capturing the fine details present in the image. Furthermore, NSCT provides a sparse representation of signals and structurally conforms to the frequency sensitivity distribution of the HVS. These facts motivate us to utilize NSCT to develop our proposed MIF scheme.

III. Reduced Pulse Coupled Neural Network

PCNN is a single layered, 2-D, laterally connected neural network of pulse-coupled neurons [12], [14]. The neuron consists of an input part (dendritic tree), linking part, and a pulse generator as shown in Fig. 2. The neuron receives the input signals from feeding and linking inputs. Considering the applications of multimodal MIF, and in order to improve the computational efficiency (in terms of reducing the number of optimizable parameters), we use an RPCNN model adapted slightly from [22]:

$$F_{i,j}[n] = S_{i,j} \tag{1}$$

$$L_{i,j}[n] = \sum_{k,l} W_{i,j,k,l} Y_{i,j}[n-1] \tag{2}$$

$$U_{i,j}[n] = F_{i,j}[n](1 + \beta L_{i,j}[n]) \tag{3}$$

$$Y_{i,j}[n] = \begin{cases} 1, & U_{i,j}[n] > T_{i,j}[n-1] \\ 0, & \text{otherwise} \end{cases} \tag{4}$$

$$T_{i,j}[n] = e^{-\alpha_T} T_{i,j}[n-1] + V_T Y_{i,j}[n] \tag{5}$$

where the indexes i and j refer to the pixel (coefficient) location in the image. k and l refer to the dislocation in a symmetric neighborhood around a pixel (coefficient), and n denotes the current iteration. F and L are called feeding and linking inputs, respectively. $W_{i,j,k,l}$ represents the synaptic weight coefficient and $S_{i,j}$ denotes the external stimulus. The linking modulation is given in (3), where $U_{i,j}[n]$ is the internal state of the neuron and β is the linking strength parameter. The pulse generator determines the firing events in the model in (4). The value of $Y_{i,j}[n]$ depends on the internal state and threshold. The dynamic threshold of the neuron is given in (5), where V_T and α_T are the normalized constant and time constant, respectively.

Compared to the nine parameters of the standard PCNN model, the RPCNN contains only four key parameters: $W_{i,j,k,l}$, $\beta_{i,j}$, V_T, and α_T (for details, see [12], [14], [22]). Moreover, $W_{i,j,k,l}$ is usually kept unchanged and we set these to the reciprocal of the square distance between two pixels (coefficients). Among the remaining three parameters, the linking coefficient β can vary the weighting of the linking channel in the internal activity, and hence is application dependent. Keeping this in mind, we propose to adaptively set the values of the linking strengths β, based on the fuzzy-logic approach, and set the values of the other two parameters, heuristically.

IV. Proposed Method

In the proposed method, coefficients of both the low-frequency subbands (LFSs) and high-frequency subbands (HFSs) are fused in a similar way using RPCNNs with fuzzy-adaptive linking strengths. The notations used are as follows: $I = (P, Q, R)$ where P, Q, R represent the two source images and the resultant fused image, respectively. The value $B^I_{s,d}(i,j)$ indicates a coefficient of the subband B of the image I at the scale s $(= 1, \ldots, S)$ and direction d, where S is the coarsest scale, and (i,j) denotes the spatial location of the coefficient in the subband. This method can be easily extended to more than two images.

A. Fuzzy Adaptive Linking Strength

From the PCNN-related literature, we know that the linking strength (β) reflects the pixel's (coefficient) characteristics, and should be adaptive to the importance (significance) of the corresponding pixel (coefficient). Moreover, from the HVS-model-related literature, it has been found that the contrast enhancement mechanism and the incremental visual threshold can be effectively modeled as a nonlinear system, which following the HVS decides the visually significant or insignificant pixels with respect to its neighbors [18], [23], [24]. The uncertainty exists in deciding the visual quality (significance) of the image's pixel (coefficient) and the subjectivity of the HVS response is successfully handled by the fuzzy-logic approaches [19], [25].

Keeping these in mind, we propose to use a novel fuzzy-based technique to adaptively set the value of β by estimating each coefficient's significance (importance) in the corresponding image. If a coefficient's "local average energy (LAE)" is large or its "local information entropy (LIE)" is large, then the coefficient has more importance in the image. We consider $\text{LAE}^I_{s,d}(i,j)$ and $\text{LIE}^I_{s,d}(i,j)$ as the representations of a coefficient's "local average energy" and its "local information entropy", respectively. LAE gives the information about the existence of edges, contours, and textures in an image. Similarly, LIE indicates the complexity or unpredictability of a local region. The regions corresponding to high-signal complexity tend to have flatter distributions and hence higher entropy, and these regions are considered to be the important regions (edges, contours, and texture information) of the image [26].

For a coefficient $B^I_{s,d}(i,j)$, $\text{LAE}^I_{s,d}(i,j)$ and $\text{LIE}^I_{s,d}(i,j)$ are computed according to (6) and (7), respectively, considering a window of size $M \times N$ centered around the coefficient:

$$\text{LAE}^I_{s,d}(B^I_{s,d}(i,j)) = \frac{1}{M \times N} \sum_{m=1}^{M} \sum_{n=1}^{N} B^I_{s,d}(m,n)^2 \tag{6}$$

$$\text{LIE}(B^I_{s,d}(i,j)) = -\sum p(B^I_{s,d}(i,j)) \log_2 p(B^I_{s,d}(i,j)) \tag{7}$$

where $p(B^I_{s,d}(i,j))$ is the probability of occurrence of the coefficient $B^I_{s,d}(i,j)$.

The fuzzy membership values $\mu_1(B^I_{s,d}(i,j))$ and $\mu_2(B^I_{s,d}(i,j))$ corresponding to $\text{LIE}^I_{s,d}(i,j)$ and $\text{LIE}^I_{s,d}(i,j)$, respectively are computed as follows:

$$\mu_1(B^I_{s,d}(i,j)) = \begin{cases} 0, & \text{LAE}^I_{s,d}(i,j) \le a_1 \\ 2\left(\frac{\text{LAE}^I_{s,d}(i,j) - a_1}{c_1 - a_1}\right)^2, & a_1 \le \text{LAE}^I_{s,d}(i,j) \le b_1 \\ 1 - 2\left(\frac{\text{LAE}^I_{s,d}(i,j) - a_1}{c_1 - a_1}\right)^2, & b_1 \le \text{LAE}^I_{s,d}(i,j) \le c_1 \\ 1, & \text{LAE}^I_{s,d}(i,j) \ge c_1 \end{cases} \tag{8}$$

and

$$\mu_2(B^I_{s,d}(i,j)) = \begin{cases} 0, & \text{LIE}^I_{s,d}(i,j) \le a_2 \\ 2\left(\frac{\text{LIE}^I_{s,d}(i,j) - a_2}{c_2 - a_2}\right)^2, & a_2 \le \text{LIE}^I_{s,d}(i,j) \le b_2 \\ 1 - 2\left(\frac{\text{LIE}^I_{s,d}(i,j) - a_2}{c_2 - a_2}\right)^2, & b_2 \le \text{LIE}^I_{s,d}(i,j) \le c_2 \\ 1, & \text{LIE}^I_{s,d}(i,j) \ge c_2 \end{cases} \tag{9}$$

where $b_1 = \text{average}(\text{LAE}^I_{s,d})$, $c_1 = b_1 + \max(|b_1 - \max(\text{LAE}^I_{s,d})|, |b_1 - \min(\text{LAE}^I_{s,d})|)$, $a_1 = 2b_1 - c_1$, and similarly, $b_2 = \text{average}(\text{LIE}^I_{s,d})$, $c_2 = b_2 + \max(|b_2 - \max(\text{LIE}^I_{s,d})|, |b_2 - \min(\text{LIE}^I_{s,d})|)$, $a_2 = 2b_2 - c_2$. Here, b_k is the cross-over

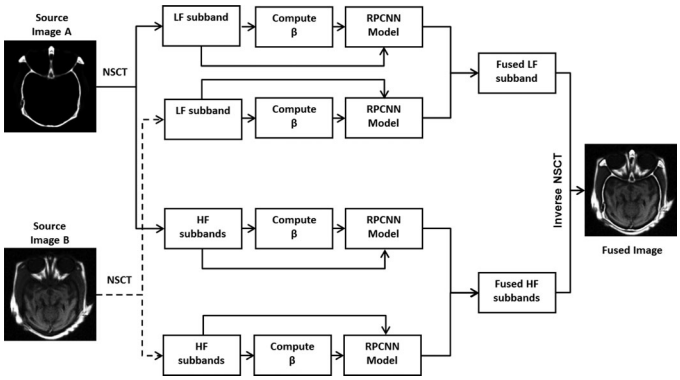

Fig. 3. Block Diagram of the proposed MIF method.

point, c_k is the shoulder point, and a_k is the feet point of S-type membership curve, $k = 1, 2$ (considering the two source images).

The linking strength $\beta_{i,j}^{s,d,I}$ corresponding to the coefficient $B_{s,d}^{I}(i,j)$ is then computed as follows:

$$\beta_{i,j}^{s,d,I} = \max(\mu_1(B_{s,d}^{I}(i,j)), \mu_2(B_{s,d}^{I}(i,j))). \quad (10)$$

B. Algorithm

Assuming that the medical images to be fused are coregistered to ensure that the corresponding pixels are aligned, here we outline the salient steps of the proposed MIF method.

1) Decompose the registered source medical images P and Q by NSCT to get the LFSs and HFSs.
2) Compute the linking strengths $\beta_{i,j}^{s,d,I}$, $I = (P, Q)$ as described in Section IV-A.
3) Input the coefficients of the subbands to motivate the RPCNNs and generate pulse of neurons using (1)–(5), and compute the firing times $G_{s,d}^{I}(i,j) = \sum_{n=1}^{N} Y_{i,j}^{s,d,I}[n]$, $I = (P, Q)$.
4) At $n = N$ (total number of iterations), determine the fused coefficient $B_{s,d}^{R}(i,j)$ following the fusion rule:

$$B_{s,d}^{R}(i,j) = \begin{cases} B_{s,d}^{P}(i,j), & G_{s,d}^{I}(i,j) \geq G_{s,d}^{I}(i,j) \\ B_{s,d}^{Q}(i,j), & \text{otherwise} \end{cases}. \quad (11)$$

5) Apply inverse NSCT on the fused coefficients to get the final fused medical image R.

The block diagram of the proposed MIF scheme is shown in Fig. 3.

V. Experimental Results and Comparisons

To evaluate the performance of the proposed technique, extensive experiments were carried out on five different groups of medical images combining different modalities (CT/MRI, T1_W_MR/MRA, FLAIR/diffusion-weighted (DW), FDG_PET/MR, and FDG_PET/CT). Each group contains at least seven image pairs: one pair from one patient and one slice per image. For simplicity, we term the proposed neuro-fuzzy hybrid MIF method based on the NSCT as NFHF-NSCT.

A. Experimental Setup

We implemented the proposed technique in MATLAB, and experiments were done on a PC with 2.66-GHz CPU and 4-GB RAM. Parameters of PCNN were set as $k \times l = 3 \times 3$, $\alpha_T = 0.2$, $V_T = 20$, $W = [0.7071\ 1\ 0.7071; 1\ 0\ 1; 0.7071\ 1\ 0.7071]$, and $N = 200$. The size of the window for computing the LAE and the LIE was set as 3×3.

The selected quantitative criterions used in the objective analysis are described next briefly. Standard deviation (STD) is used to measure the image contrast (high STD means better contrast). To measure the image information content, entropy (EN) is used. If EN of the fused image is higher than the source images, then it indicates that the fused image contains more information. Spatial frequency (SF) is used to measure the overall activity and clarity level of an image. Larger SF value denotes better fusion result. Mutual information (MI) measures the degree of dependence of the two images. A larger MI implies better quality [27]. The other objective IF performance measures used in the experiments are $Q^{AB/F}$ and Q_0 [28]. Values of both of these two measures should be near to 1, which indicate a better fused image.

The visual and quantitative results for five pairs of source images from the five different combinations described previously are given in this section. For simplicity, we have termed the five pairs of source medical images as "Group 1" to "Group 5", and these are shown in the first two columns of Fig. 4. In "Group 1," the CT image in Fig. 4(a1) shows the bone structure, and the MRI image in Fig. 4(b1) displays the soft tissue information. The T1-weighted MR image in Fig. 4(a2) contains the soft tissues, and a lesion in the brain, but the vascular nature of the lesion is not clear. The vascular nature of the lesion is evident in the MRA image of Fig. 4(b2), but the tissue information is low. The fluid attenuated inversion recovery (FLAIR) MR image of Fig. 4(a3) shows a symmetrical signal hyperintensity of the occipito-parietal cortical ribbon, and the DW image of Fig. 4(b3) shows an increased signal in the areas of the FLAIR abnormality. In Fig. 4(a4), the coronal F-18 fluorodeoxyglucose (FDG)-PET image provides the metabolic information, whereas, the coronal MR-T1 image of Fig. 4(b4) shows the structural information. The FDG-PET image of Fig. 4(a5) shows a lesion in the right lung that indicates increased FDG uptake, and the CT image of Fig. 4(b5) shows the structural information with the exact location of the lesion within the right lung. We have compared our proposed method with five state-of-the-art MIF schemes both subjectively and objectively. The performance of the proposed NFHF-NSCT method is also compared with the effectiveness of other MGA-tools such as contourlet (CNT) and curvelet (CVT). Even though we provide the visual and quantitative results for five pairs of medical images, for the other source images we have got similar results.

B. Subjective Analysis and Discussion

An expert radiologist was asked to subjectively evaluate the effectiveness of the proposed method. Both the fused images obtained by our proposed method, and the fused images obtained by the compared schemes were shown to the radiologist.

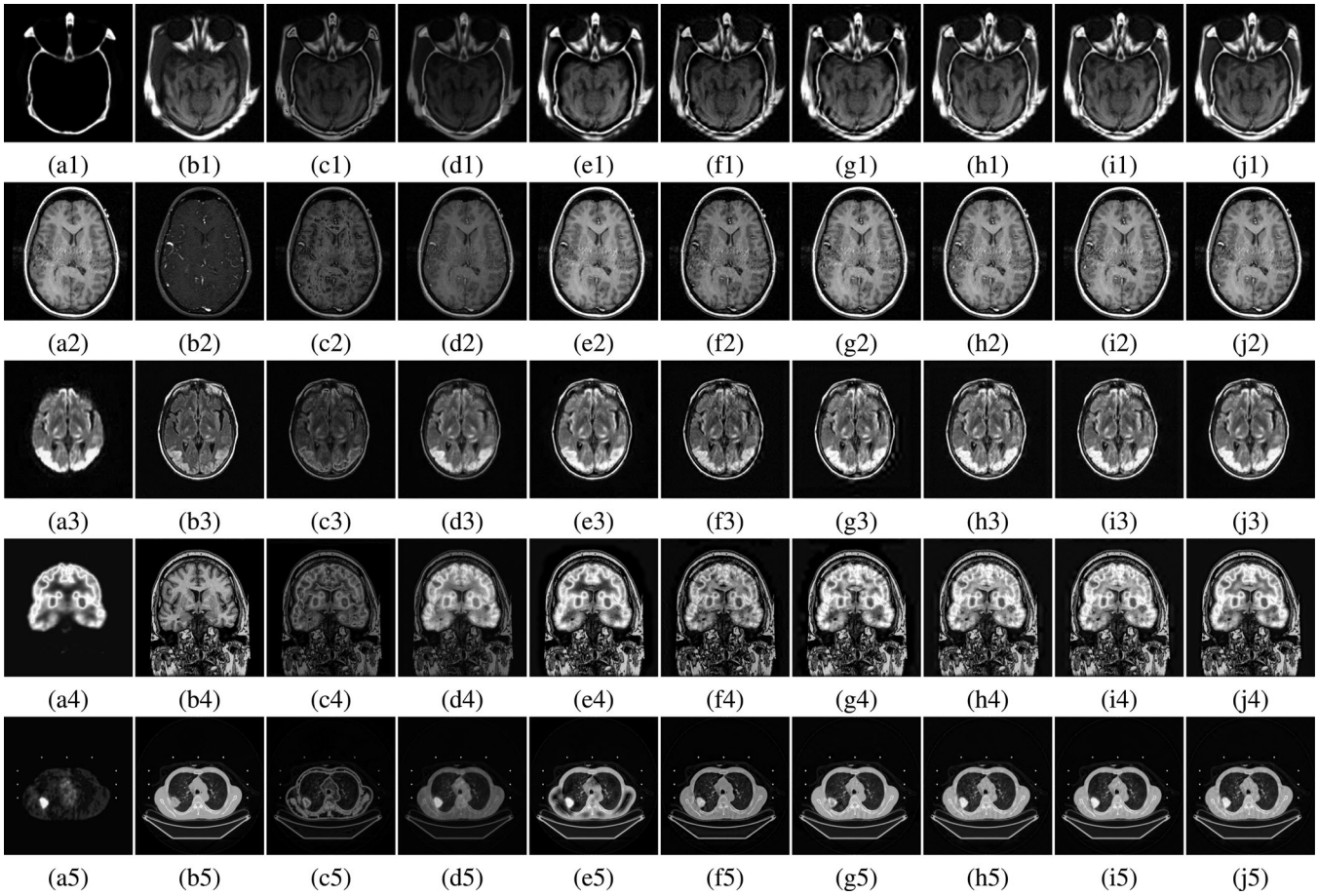

Fig. 4. Visual results for the five pairs (ak, bk) of source images, (k = 1, 2, 3, 4, 5). Fused images obtained: (c1)–(c5) by scheme [7], (d1)–(d5) by scheme [5], (e1)–(e5) by scheme [15], (f1)–(f5) by scheme [9], (g1)–(g5) by scheme [6], (h1)–(h5) by NFHF-CNT, (i1)–(i5) by NFHF-CVT, (j1)–(j5) by the proposed scheme.

According to the clinician opinion, it can be seen from the given results of Fig. 4, that apart from our proposed method [see Fig. 4 (j1)–(j5)] and the schemes of [6] [see Fig. 4 (g1)–(g5)] and [15] [see Fig. 4 (e1)–(e5)], all the other compared techniques suffer from the problem of contrast reduction. Moreover, he found that the fused images obtained by the schemes of [7] [see Fig. 4 (c1)–(c5)], [15] [see Fig. 4 (e1)–(e5)], [9] [see Fig. 4 (f1)–(f5)], and [6] [see Fig. 4 (g1)–(g5)] have lost large amount of image details. Furthermore, he observed that the methods of [9] [see Fig. 4 (f1)–(f5)] and [6] [see Fig. 4 (g1)–(g5] suffer from the problem of blocking effect (as evident from the lower portions of the images) and contain unwanted image degradations, whereas, in his opinion, the fused image Fig. 4(j1) obtained by our proposed scheme for "Group 1" source images, contains both the bone structure [from the CT image of Fig. 4(a1)] and the soft tissue information [from the MRI image of Fig. 4(b1)]. The lesion and its vascular nature along with the soft tissue information are evident in the fused image Fig. 4(j2) of "Group 2." Both the complementary information from the source images of "Group 3" can be clearly seen in the fused image Fig. 4(j3). For "Group 4", the fused image shown in Fig. 4(j4) contains the metabolic information from the FDG-PET image of Fig. 4(a4) and the structural information from the T1-weighted MR image of Fig. 4(b4). The fused image of Fig. 4(j5) of "Group 5" shows both the structural information (exact location) and the metabolic activity of the lesion in the same image. Finally, after careful inspection of all the resultant images, the clinician agreed to the effectiveness of the proposed scheme. He found that the fused images obtained by the proposed scheme are clearer, informative, and have higher contrast than the source medical images. For evaluating the efficiency of the NSCT over CNT and CVT (termed as NFHF-CNT and NFHF-CVT, respectively in the paper), we also showed the zoomed-in versions of the fused images to the clinician. The zoomed-in version resultant images of "Group 1" images, obtained by NFHF-CNT, NFHF-CVT, and NFHF-NSCT, are shown in Fig. 5. The clinician agreed that even though the fused images obtained by NFHF-CNT and NFHF-CVT look similar to the fused images produced by our proposed technique, both of these transforms

Fig. 5. Performance comparison of CNT, CVT, and NSCT. Zoomed in the versions of "Group 1" fused images of Fig. 4 (a) h1 for CNT, (b) i1 for CVT, and (c) j1 for NSCT.

TABLE I
PERFORMANCE EVALUATION OF THE PROPOSED SCHEME

Group	Source Image				Fused Image		
	No.	SF	EN	STD	SF	EN	STD
1	a1	4.4316	1.7126	44.7519	**7.2512**	**6.7918**	**64.6989**
	b1	6.2600	5.6013	58.8283			
2	a2	7.7005	4.1524	**69.1972**	**7.9600**	**6.3514**	69.1150
	b2	6.4901	4.3310	25.5812			
3	a3	10.4970	2.4263	59.7992	10.5607	**5.8155**	**64.4903**
	b3	**12.7502**	2.6375	49.6101			
4	a4	5.1728	3.2840	67.1263	**9.5685**	**6.6329**	**74.2056**
	b4	9.3992	5.3682	64.4280			
5	a5	2.8705	1.9766	19.8552	**5.8448**	**4.9837**	56.5273
	b5	5.6831	5.0498	**56.8748**			

cause blurring of edges and unwanted image degradations as shown in Fig. 5. We can clearly see from the resultant images given in Fig. 4 and Fig. 5 that the proposed MIF method results in the low contrast reduction, high clarity, and high information content. The proposed MIF scheme also causes less unwanted degradations in the fused images, as well as is free from the problem of blocking effect.

C. *Objective Analysis and Discussion*

For the five pairs of source medical images, the detailed quantitative evaluations are given in Table I. Columns 3 to 5 in Table I, show the SF, EN, and STD of the source medical images, respectively. The values of these quantitative measures of the fused images obtained by the proposed technique are given in columns 6 to 8 of Table I. The "bold" values indicate the highest values in Table I, for that quantitative measure. The highest values of SF for the images of Groups 1, 2, 4, and 5 indicate that the fused images obtained by our proposed method have more activity and clarity level than the source images. Similarly, the highest values of EN for the fused images indicate that the fused images obtained by the proposed scheme have more information content than the source images. We can also see from Table I that the STD values of the fused images for three out of five source image combinations are higher than their corresponding source images. This shows that the proposed method produces higher contrast fused images. Only in the case of image Groups 2 and 5, the STD values of one of the corresponding source images [see Fig. 4(a2) and Fig. 4((b5)] are greater than the fused images. It may be because of the fact that the other source images [see Fig. 4(b2) and 4(a5)] of the image Groups 2 and 5 have very low contrast (indicated by the low STD values), causing the fused images to have lower STD values (lower by very small amount). Therefore, it is evident from Table I, that the fused images obtained by the proposed method are more clear, informative, and have higher contrast which is helpful in visualization and interpretation.

The quantitative performance comparisons of our proposed method against some of the existing MIF schemes are given in the Fig. 6 in form of "error bar" plots. Fig. 6 shows the average and the STD values of the different measures used in the experiments for all the seven pairs of source images for all the five different groups. We can see from Fig. 6 that the proposed scheme has all the largest objective measures (five out of six),

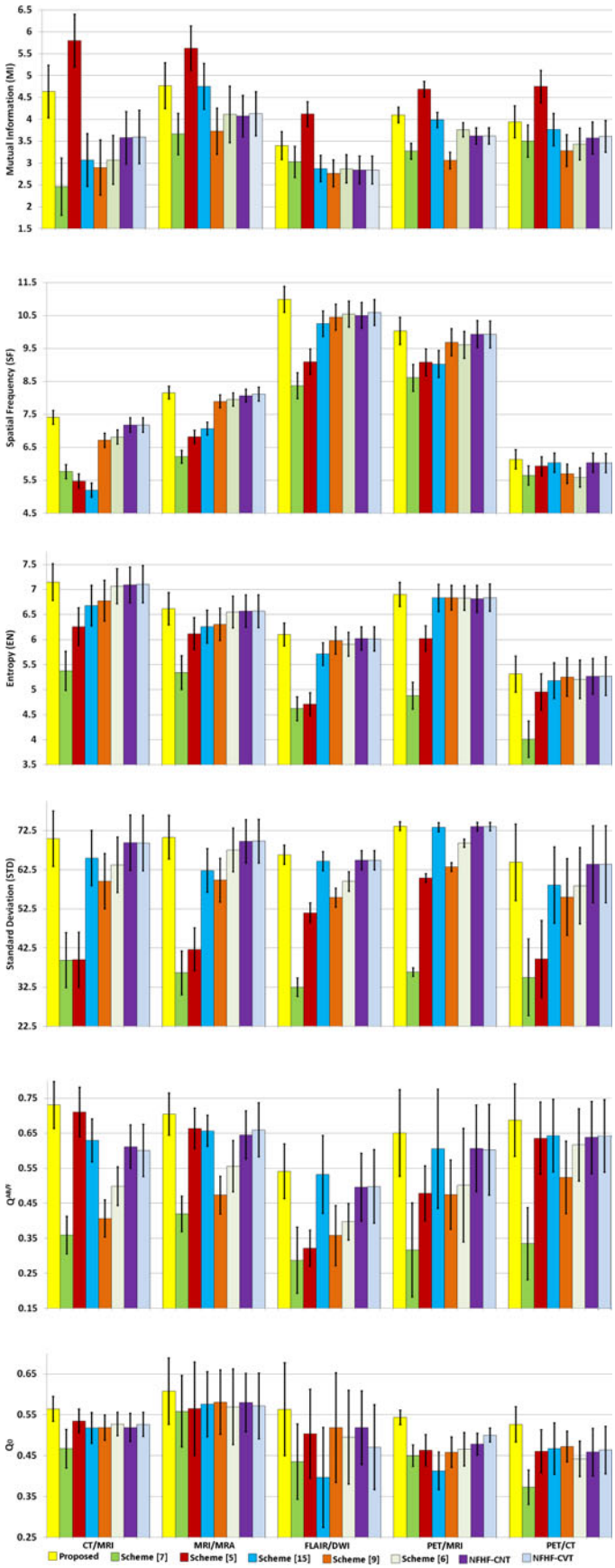

Fig. 6. Objective performance comparisons.

which is obviously better than the other methods. The highest values of SF indicate that the fused images obtained by our proposed method have more activity and clarity level than the other schemes. Similarly, the highest values of EN and STD for the fused images show that the fused images obtained by the proposed scheme have more information, as well as higher contrast than the other compared methods. It is also clear that the method in [5] is better than our proposed scheme in view of the quantitative measure MI. But our proposed scheme is superior for all the other quantitative measures. Moreover, the RPCNN used in the proposed technique having less complex structure and parameters is computationally efficient than the original PCNN. This helps in reducing the computational cost of the overall system. Specifically, the proposed technique requires approximately 45 to 55 seconds to fuse a pair of source medical images of size 512×512, irrespective of their modalities. Therefore, it is obvious from the obtained results that the fused images obtained by the proposed MIF method based on the hybrid neuro-fuzzy technique and NSCT are more clear, informative, and have higher contrast than the existing mentioned MIF methods.

VI. Conclusion

We propose a novel MIF method based on a hybrid neuro-fuzzy approach in the NSCT domain. To overcome the drawbacks of the traditional MIF schemes, and to integrate as much information as possible into the fused images, we exploit the advantages of the NSCT, RPCNN, and fuzzy logic. The linking strengths of the neurons in the RPCNNs are adaptively computed based on the fuzzy characteristics of the image, which results in high-quality fused images. The experimental results show that the proposed method can preserve more useful information in the fused image with higher spatial resolution and less difference to the source images. The effects of the different fusion rules, as well as the new techniques to compute the parameters of the neurons of the PCNN, are some of the future scopes of the proposed technique.

Acknowledgment

The authors would like to thank Dr. P. K. Das (Medicare Images, Asansol-4, West Bengal, India) for providing us some of the source medical images and for the subjective evaluation of the fusion results. They would also like to thank http://www.imagefusion.org/ and http://www.med.harvard.edu/aanlib/home.html for providing us the source medical images.

References

[1] B. Solaiman, R. Debon, F. Pipelier, J. M. Cauvin, and C. Roux, "Information fusion: Application to data and model fusion for ultrasound image segmentation," *IEEE Trans. Biomed. Eng.*, vol. 46, no. 10, pp. 1171–1175, Oct. 1999.

[2] V. Barra and J. Y. Boire, "A general framework for the fusion of anatomical and functional medical images," *NeuroImage*, vol. 13, no. 3, pp. 410–424, 2001.

[3] S. Das and M. K. Kundu, "NSCT-based multimodal medical image fusion using pulse-coupled neural network and modified spatial frequency," *Med. Biol. Eng. Comput.*, vol. 50, no. 10, pp. 1105–1114, 2012.

[4] V. S. Petrovic and S. Xydeas, "Gradient-based multiresolution image fusion," *IEEE Trans. Image Process.*, vol. 13, no. 2, pp. 228–237, Feb. 2004.

[5] Z. Wang and Y. Ma, "Medical image fusion using m-PCNN," *Inf. Fusion*, vol. 9, no. 2, pp. 176–185, Apr. 2008.

[6] Y. Yang, D. S. Park, S. Huang, and N. Rao, "Medical image fusion via an effective wavelet-based approach," *EURASIP J. Adv. Signal Process.*, vol. 2010, pp. 44:1–44:13, 2010.

[7] H. Tian, Y.-N. Fu, and P.-G. Wang, "Image fusion algorithm based on regional variance and multi-wavelet bases," in *Proc. 2nd Int. Conf. Future Comput. Commun.*, 2010, vol. 2, pp. 792–795.

[8] G. Pajares and J. M. de la Cruz, "A wavelet-based image fusion tutorial," *Pattern Recognit.*, vol. 37, no. 9, pp. 1855–1872, 2004.

[9] L. Yang, B. L. Guo, and W. Ni, "Multimodality medical image fusion based on multiscale geometric analysis of contourlet transform," *Neurocomputing*, vol. 72, nos. 1–3, pp. 203–211, 2008.

[10] S. Das, M. Chowdhury, and M. K. Kundu, "Medical image fusion based on ripplet transform type-I," *Progr. Electromagn. Res. B*, vol. 30, pp. 355–370, 2011.

[11] R. Eckhorn, H. J. Reitboeck, M. Arndt, and P. Dicke, "Feature linking via synchronization among distributed assemblies: Simulations of results from cat visual cortex," *Neural Comput.*, vol. 2, pp. 293–307, 1990.

[12] F. C. Z. Wang, Y. Ma, and L. Yang, "Review of pulse-coupled neural networks," *Image Vis. Comput.*, vol. 28, no. 1, pp. 5–13, 2010.

[13] J. L. Johnson, "Time signatures of images," in *Proc. IEEE Neural Netw.*, 1994, vol. 2, pp. 1279–1284.

[14] J. Johnson and M. Padgett, "PCNN models and applications," *IEEE Trans. Neural Netw.*, vol. 10, no. 3, pp. 480–498, May 1999.

[15] Q. Xiao-Bo, Y. Jing-Wen, X. Hong-Zhi, and Z. Zi-Qian, "Image fusion algorithm based on spatial frequency-motivated pulse coupled neural networks in nonsubsampled contourlet transform domain," *Acta Automatica Sinica*, vol. 34, no. 12, pp. 1508–1514, 2008.

[16] Z. Wang, Y. Ma, and J. Gu, "Multi-focus image fusion using PCNN," *Pattern Recognit.*, vol. 43, no. 6, pp. 2003–2016, Jun. 2010.

[17] J. M. Kinser, "Foveation by a pulse-coupled neural network," *IEEE Trans. Neural Netw.*, vol. 10, no. 3, pp. 621–626, 1999.

[18] M. K. Kundu and S. K. Pal, "A note on the transformation between intensity and gray level," *Pattern Recognit. Lett.*, vol. 8, pp. 257–269, 1988.

[19] M. K. Kundu and S. K. Pal, "Automatic selection of object enhancement operator with quantitative justification based on fuzzy set theoretic measure," *Pattern Recognit. Lett.*, vol. 11, pp. 811–829, 1990.

[20] J. M. Kinser, "Pulse coupled image fusion," *Opt. Eng.*, vol. 36, no. 3, pp. 737–742, 1997.

[21] A. da Cunha, J. Zhou, and M. Do, "The nonsubsampled contourlet transform: Theory, design, and applications," *IEEE Trans. Image Process.*, vol. 15, no. 10, pp. 3089–3101, Oct. 2006.

[22] J. A. Karvonen, "Baltic sea ice SAR segmentation and classification using modified pulse-coupled neural networks," *IEEE Trans. Geosci. Remote Sens.*, vol. 42, no. 7, pp. 1566–1574, Jul. 2004.

[23] G. Buchsbaum, "An analytical derivation of visual nonlinearity," *IEEE Trans. Biomed. Eng.*, vol. 27, no. 5, pp. 237–242, May 1980.

[24] M. K. Kundu and S. K. Pal, "Thresholding for edge detection using human psycho visual phenomena," *Pattern Recognit. Lett.*, vol. 4, pp. 433–441, 1986.

[25] H. Cheng and H. Xu, "A novel fuzzy logic approach to contrast enhancement," *Pattern Recognit.*, vol. 33, no. 5, pp. 809–819, 2000.

[26] T. Kadir and M. Brady, "Saliency, scale and image description," *Int. J. Comput. Vis.*, vol. 45, no. 2, pp. 83–105, 2001.

[27] G. H. Qu, D. L. Zhang, and P. F. Yan, "Information measure for performance of image fusion," *Electron. Lett.*, vol. 38, no. 7, pp. 313–315, 2002.

[28] C. S. Xydeas and V. Petrovic, "Objective image fusion performance measure," *Electron. Lett.*, vol. 36, no. 4, pp. 308–309, 2000.